Supreet S. Bahga[2]
Moran Bercovici[1]
Juan G. Santiago[2]

[1]Department of Aeronautics and Astronautics, Stanford University, Stanford, CA, USA
[2]Department of Mechanical Engineering, Stanford University, Stanford, CA, USA

Received September 17, 2009
Revised November 18, 2009
Accepted November 29, 2009

Research Article

Ionic strength effects on electrophoretic focusing and separations

We present a numerical and experimental study of the effects of ionic strength on electrophoretic focusing and separations. We review the development of ionic strength models for electrophoretic mobility and chemical activity and highlight their differences in the context of electrophoretic separation and focusing simulations. We couple a fast numerical solver for electrophoretic transport with the Onsager–Fuoss model for actual ionic mobility and the extended Debye–Huckle theory for correction of ionic activity. Model predictions for fluorescein mobility as a function of ionic strength and pH compare well with data from CZE experiments. Simulation predictions of preconcentration factors in peak mode ITP also compare well with the published experimental data. We performed ITP experiments to study the effect of ionic strength on the simultaneous focusing and separation. Our comparisons of the latter data with simulation results at 10 and 250 mM ionic strength show the model is able to capture the observed qualitative differences in ITP analyte zone shape and order. Finally, we present simulations of CZE experiments where changes in the ionic strength result in significant change in selectivity and order of analyte peaks. Our simulations of ionic strength effects in capillary electrophoresis compare well with the published experimental data.

Keywords:
Capillary electrophoresis / Ionic strength / ITP / Separation / Simulation
DOI 10.1002/elps.200900560

1 Introduction

1.1 General aspects

Electrophoretic separation and preconcentration techniques such as CZE and ITP are widely used as analytical tools in a variety of fields, including drug discovery, toxin detection, genetics and food analysis [1, 2]. These techniques rely on differences in electrophoretic mobilities of analytes to separate them in the presence of an electric field. The analytes can be weak or strong acids and bases, or can be amphoteric and posses both anionic and cationic groups. The degree of dissociation of such analytes is typically a function of their dissociation constants (pK_a), local pH and local ionic strength. The degree of dissociation determines the degree of ionization (or effective charge) of the species and can be linked directly to its effective mobility. The dependence of effective ionic mobility on pH and pK_a is described in detail in [3–8]. There are several models with varying complexity [9–13] for predicting the fully ionized mobility (actual ionic mobility) of ions (*e.g.* a singly ionized weak acid at a pH, a few units above the pK_a) at finite ionic strengths, given their limiting mobility at zero ionic strength (*i.e.* the infinite dilution limit). In addition, activity coefficients vary with ionic strength, leading to a change in ionization and effective mobility [8]. In general, effective, observable ion mobility at finite ionic strength depends on the limiting fully ionized mobility of the ion, the mobility of its counter- and co-ions, ionic charge (valence values), buffer composition and ion dissociation constants (*e.g.* pK_a values).

Several experimental studies have underlined the importance of ionic strength in separations and have leveraged its understanding for improving the design of assays. For example, electrophoretic separations at high ionic strengths have been suggested to minimize peak distortion due to electromigration dispersion [14], and high ionic strength separations have also been used to reduce wall adsorption of cationic proteins [15] and increased analyte selectivity [16]. Other studies have reported on the adverse effects of high ionic strength, which may lead to zone reversal in CZE and ITP [17, 18], and decreased focusing rate in ITP [19].

Correspondence: Professor Juan G. Santiago, Associate Professor, 440 Escondido Mall, Building 530, Room 225, Stanford, CA 94305, USA
E-mail: juan.santiago@stanford.edu
Fax: +1-650-723-7657

Abbreviations: AF, Alexa–Fluor 488**; LE,** leading electrolyte**; NFT,** non-focusing tracer**; OGCA,** Oregon green carboxylic acid**; R6G,** rhodamine 6G**; TE,** terminating electrolyte

These practical consequences underline the importance of the influence of ionic strength on ionic mobility in modeling electrophoretic focusing and separation. Numerical simulations can minimize the number of required experimental runs for choosing optimal conditions; can be used to design and perform at least preliminary optimizations of assays; and are a useful tool in evaluating experiments and elucidating underlying physicochemistry processes. Ionic strength models and calculations have been offered by and incorporated in the capillary electrophoresis solver Peakmaster [20], which solves for the chemical properties of a uniform buffer, as well as in the full electrophoresis simulation code Simul [21]. In [20], the authors have provided a validation of Peakmaster by comparing computed results for several equilibrium buffer compositions with experimental measurements. However, significant (and sometimes prohibitive) computational costs associated with ionic strength-dependent calculations in numerical simulations have to date often limited their usefulness in electrophoretic separation research and practice. In [21], for example, the authors have noted that the simulations were conducted with the ionic strength model disabled in order to reduce the computational time. Thus, stimulation of the effect of ionic strength on separations and focusing was not reported in that study.

In this study, we present the implementation and experimental validation of an ionic strength model in a fast numerical solver for electrophoretic transport. We correct for ionic strength effects using the Onsager–Fuoss model [9] and extended Debye–Huckle theory [22] for correction of ionic activity. We validate the ionic strength corrections with ionic mobility measurements of fluorescein in CZE. We also use simulations and experiments to demonstrate and analyze the influence of ionic strength on focusing and zone order in ITP. We also use our model to demonstrate a case of changes in selectivity and peak reversal in CZE (*i.e.* a change of the order of peaks in an electropherogram), by varying ionic strength.

1.2 Mathematical model for fully ionized mobility

We can define the ''fully ionized'' mobilities (actual ionic mobility) of an ion in solution as the mobilities the ion would take on with integer values of its valence. For example, the ion A^- takes on its fully ionized mobility for aqueous solutions of the singly ionized (single pK_a) acid HA at sufficiently high pH. A weak acid with two nearby pK_a values at charge –1 and –2 may never realize its fully ionized mobility associated with the –1 charge state, but we can still define such fully ionized mobility mathematically [8]. The presence of an ionic atmosphere around the ion in solution at finite ionic strength results in reduced actual mobility compared with mobility of an isolated ion (at zero ionic strength).

We here summarize the following models describing the effect of ionic strength on the fully ionized mobility of ions: Kohlraush [13], Onsager [23, 24], Onsager and Fuoss [9] and Pitts [10]. We discuss the differences between these models and present their associated mathematical relationships, with the exception of Pitts' model [10],] whose formulation is fairly complex and does not provide additional insight in this discussion. We summarize the source, assumptions, equations and descriptions of these models in Supporting Information Table S1.

Onsager derived a theory for the dependence of conductivity of a strong electrolyte on concentration, based on the ionic atmosphere model of Debye and Huckle [22, 25]. Onsager's theoretical model [23, 24] is functionally equivalent to Kohlrausch's empirical model [13] for conductivity of an electrolyte at finite ionic strength. The latter is given by $\Lambda = \Lambda_0 - k\sqrt{c}$, where Λ is the molar conductivity, Λ_0 its value at infinite dilution, c the ion concentration and k an empirical constant. Onsager's model treats ions as point charges and is restricted to dilute electrolytes containing two fully ionized species of opposite charges. This original theory for conductivity at finite ionic strength can be expressed in terms of electrophoretic mobility μ as,

$$\mu_i = \mu_i^0 - (A\mu_i^0 + B)\sqrt{c} \tag{1}$$

where μ_i^0 denotes the limiting ionic mobility of the species i at zero ionic strength (for a given integer value of valence) and c the concentration of the solute. The reduction in mobility can be attributed primarily to two factors. First, an ion in solution attracts a cloud of counter-ions (ionic atmosphere) around itself, balancing local charge. Under an applied electric field, the ion and its counter-ionic cloud move in opposite direction and this causes a polarization (new counter-ions are recruited and old ions are rejected, but overall the ion and its ionic atmosphere polarize). This polarization has a finite relaxation time scale – equivalent to the time scale required for the ion cloud to again reach spherical symmetry for a rapidly deactivated electric field. This so-called relaxation effect is captured by the factor A in Eq. (1). The second effect is associated with the drag force exerted by the moving counter-ion cloud ionic atmosphere on the central ion. This second effect is reflected by term B in Eq. (1) and is termed as the electrophoretic effect. Detailed discussion on these effects can be found in [9, 11, 12]. Onsager's model is valid only for dilute, binary electrolytes, and a more general theory is required for ITP and CZE, where multiple species co-exist in solution. In such a system, the mobility of any ion is dependent on the presence of all other ions in solution.

Onsager and Fuoss extended the model given by Eq. (1) to account for an arbitrary mixture of ionic species as follows [9]:

$$\begin{aligned} &\mu_i = \mu_i^0 - (A\mu_i^0 + B)\sqrt{\Gamma} \\ &A = z_i \frac{e^3}{12\pi}\sqrt{\frac{N_{AV}}{(\varepsilon kT)^3}}\sum_{n=0}^{\infty} C_n R_i^n \\ &B = |z_i|\frac{e^2}{6\pi\eta}\sqrt{\frac{N_{AV}}{\varepsilon kT}}, \quad \Gamma = \sum_{i=1}^{s}\Gamma_i, \quad \Gamma_i = c_i z_i^2 \end{aligned} \tag{2}$$

Here s is the number of species, z_i the charge number of the i-th ionic species, ε the permittivity of solution, k the Boltzmann constant, e the elementary charge, N_{AV} the Avogadro constant, T the temperature of the solution and Γ the twice ionic strength, I ($I = 0.5\sum_i c_i z_i^2$). The coefficients C_n and the vectors $\mathbf{R}^n = [R_1^n, R_2^n, \ldots R_s^n]^T$ are given in [9]. However, like the Onsager model of Eq. (1), the model described by Eq. (2) again treats ions as point charges. The assumption of point charges is valid only for thick electrical double layers, where the size of the ion can be considered negligible compared with its counter-ion atmosphere. This limits the validity of Eqs. (1) and (2) to ionic strengths below order 1 mM.

At ionic strength higher than order 1 mM, finite ion size cannot be neglected. Pitts [10] provided a correction to the models of Eqs. (1) and (2) which accounts for finite ion size. The Pitts model (the relationship for which is not given here) is strictly applicable only for symmetric binary electrolytes. However, Li *et al.* [26] showed that the Pitts model is approximately equivalent to Eq. (2), with an additional term in the denominator. This forms the basis of an extended Onsager–Fuoss model given by Eq. (3), which we use in this study. We here adopt this simpler formulation, which is an extended Onsager–Fuoss model given by [20]. This extended model takes into account the finite ionic radius and arbitrary mixtures of ions:

$$\mu_i = \mu_i^0 - (A\mu_i^0 + B)\frac{\sqrt{\Gamma}}{1+\frac{aD}{\sqrt{2}}\sqrt{\Gamma}}, \quad D = \sqrt{\frac{2e^2 N_{AV}}{\varepsilon kT}} \tag{3}$$

where a represents the mean distance of closest approach for the ions. In other words, a is the distance from center of the central ion to the start of the ionic atmosphere [11]. The value of $aD/\sqrt{2}$ lies between 1 and 2 $\mathrm{mol}^{-1/2}\,\mathrm{mol}^{-3/2}$ [26]. Here (and for a wide variety of buffers), we choose a fixed value of 1.5 $\mathrm{mol}^{-1/2}\,\mathrm{mol}^{-3/2}$ as an approximation. Terms A and B in Eq. (3) are the same as those in Eq. (2). Appropriately, Eq. (3) reduces to the Robinson Stokes equation for the case of binary electrolytes [12]. Equation (3) is applicable for ionic strengths up to 100 mM [13]. We use the Onsager–Fuoss extended model, as it takes into account the relevant physics of a mixture of ions and captures, approximately, the effects of finite ion size. As examples, Fig. 1 shows variations of the fully ionized mobility of a cation for four electrolytes composed of different anion:cation pairs. We see that the reduction of mobility of divalent ions is stronger than that of univalent ions at a finite ionic strength. In addition, for the same ion, mobility reduction is higher if its counter ion bears higher charge (and thus more effectively shields the ion). The inset shows specifically the effect of finite ionic radii for a simple –1:1 electrolyte.

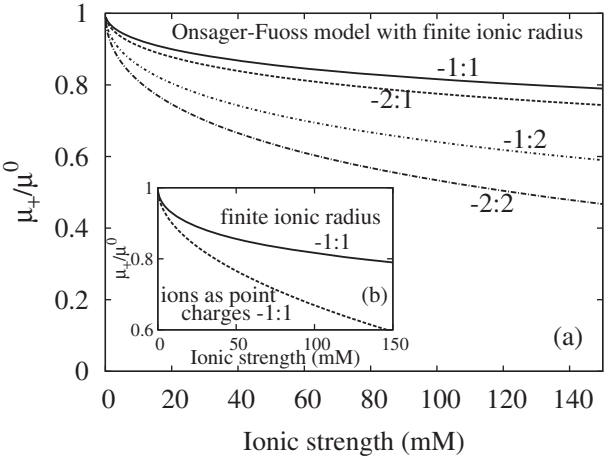

Figure 1. Mobility dependence of several binary electrolytes on ionic strength. Plot shows ionic mobility of a cation for binary electrolytes with various anion:cation valence values. (a) Variation of electrophoretic mobility of cations with ionic strength using Onsager–Fuoss model with finite ionic radius, Eq. (3). Univalent cations have lesser reduction in mobility than divalent ions for increasing ionic strength. Thus, cations in −1:1 and −2:1 electrolytes have lesser mobility, respectively, than cations in −1:2 and −2:2 electrolytes. In addition, greater charge on counter-ions (anions) causes greater reduction in mobility. Thus, cations in −2:1 and −1:2 electrolytes have lesser mobility, respectively, than cations in −1:1 and –2:2 electrolytes. (b) The effect of finite radius correction to Onsager–Fuoss model. Dotted line corresponds to Onsager–Fuoss model assuming ions as point charges, Eq. (2), and solid line corresponds to Onsager–-Fuoss model using finite ionic radius, Eq. (3). Neglecting ionic radius overpredicts the reduction in mobility at finite ionic strengths. For these sample calculations, the mobilities of all ions is taken as $\mu^0 = 50 \times 10^{-9}\ \mathrm{m^2/V/s}$.

1.3 Mathematical model for activity coefficient and degree of ionization

The observable ionic mobility of weak electrolytes (which we will call here the ''effective mobility'') depends on the degree of ionization, which can be obtained by solving for equilibrium composition of ionic species. While finite kinetic rates of reaction are sometimes important [27, 28], kinetic rates in most electrophoresis applications are faster than the characteristic times of advection and diffusion [29], and hence each species can be assumed to be in chemical equilibrium at all times. Using the notation by Stědrý *et al.* [30], the total concentration of a general ampholyte i can be expressed as the sum of its constituent ionization states:

$$c_i = \sum_{z=n_i}^{p_i} c_{i,z} \tag{4}$$

where $c_{i,z}$ is the concentration of an ionic state with valence z belonging to the species i, and n_i and p_i are the minimum and maximum valences of the species. The activities of two consecutive ionic states of species i are related by the equilibrium constant $K_{i,z}$:

$$K_{i,z} = \frac{a_{i,z}a_H}{a_{i,z+1}} = \frac{\gamma_{i,z}\gamma_H}{\gamma_{i,z+1}}\frac{c_{i,z}c_H}{c_{i,z+1}} \tag{5}$$

where c_H is the concentration of H^+ and $\gamma_{i,z}$ is the activity coefficients of z-th ionic state of species i. For dilute solutions, concentrations can be used in place of chemical

activities. However, at significant ionic strengths, activity coefficients are smaller than unity. Activity coefficients can be modeled by Debye–Huckle theory [22] with an additional term depending on ionic strength as follows:

$$\log\gamma_{i,z} = -z^2 \frac{A_{\mathrm{DH}}\sqrt{I}}{1+aD\sqrt{I}} + 0.1z^2 I, \quad I = \frac{1}{2}\sum_{i=1}^{s}\sum_{z=n_i}^{p_i} z^2 c_{i,z} \tag{6}$$

The first term is the Debye–Huckle term which accounts for long range, non-specific, electrostatic interactions. The second term represents specific interaction occurring at high ionic strength, approximated by a linear correction term. Here, A_{DH} is a temperature-dependent term and I the ionic strength in mol dm^{-3}. At room temperature A_{DH} is 0.5102 dm$^{1/2}$ mol$^{-1/2}$. Hence, in addition to reduction of (fully ionized) mobility due to ionic shielding, high ionic strength also affects the equilibrium concentrations and so the effective mobility.

For convenience, we can relate the concentrations of species with an apparent equilibrium constant

$$\tilde{K}_{i,z} \equiv \frac{\gamma_{i,z+1}}{\gamma_{i,z}\gamma_{\mathrm{H}}} K_{i,z} = \frac{c_{i,z}c_{\mathrm{H}}}{c_{i,z+1}} \tag{7}$$

These apparent equilibrium constants can then be readily used in the electroneutrality equation [7]

$$\sum_{i=1}^{s} c_i \sum_{z=n_i}^{p_i} z g_{i,z} + c_{\mathrm{H}} - \frac{\tilde{K}_w}{c_{\mathrm{H}}} = 0 \tag{8}$$

where $g_{i,z} = L_{i,z}c_{\mathrm{H}}^z / \sum_{z=n_i}^{p_i} L_{i,z}c_{\mathrm{H}}^z$ is the dissociation level of the species i, c_i is the total concentration, and $\tilde{K}_w = K_w/\gamma_{\mathrm{H}}\gamma_{\mathrm{OH}}$ is the apparent dissociation constant of water. $L_{i,z}$ depends on the apparent dissociation constants and is given by [7].

$$L_{i,z} = \begin{cases} \prod_{z'=z}^{-1} \tilde{K}_{i,z'} & z<0 \\ 1 & z=0 \\ \prod_{z'=0}^{z-1} \tilde{K}_{i,z'}^{-1} & z>0 \end{cases} \tag{9}$$

If ionic strength effects are not considered, then $L_{i,z}$ and $\tilde{K}_w$ are constants in an electrophoresis simulation. However, when ionic strength effects are considered $L_{i,z}$ and $\tilde{K}_w$ vary in space and in time as a function of the local ionic strength. To solve this system, we perform the following process at every time step of simulation. We start by taking an initial guess on the value of c_{H} (at every grid point in the domain). At the first time step, this initial guess is simply the solution for Eq. (8) with ionic strength effects neglected. For subsequent times, we use the previous solution as the new initial guess. This initial guess is used to calculate the ionic concentrations $c_{i,z}$ using $c_{i,z} = c_i g_{i,z}$ and the activity coefficients and equilibrium constants according to Eqs. (6) and (7), respectively. Equation (8) is then solved by Newton iteration, and new species concentrations $c_{i,z}$ are obtained. We repeat this process until the solution c_{H} converges to within a predefined tolerance. After converging to a solution of chemical equilibrium, the obtained ionic strength is used to calculate the fully ionized mobility, $\mu_{i,z}$, of every ionic species, using extended Onsager–Fuoss model, given by Eq. (3). This mobility is finally corrected to the effective mobility of species i by

$$\mu_i = \sum_{z=n_i}^{p_i} \mu_{i,z} g_{i,z}. \tag{10}$$

The equations evolving the dynamics of electrokinetic transport and (in the model used here) the adaptive-grid formulation are then solved for each time steps [7, 31]. The latter numerical implementation has been discussed in detail in [7, 31], and hence not repeated here.

2 Materials and methods

We performed a series of experiments to validate our model and evaluate test cases. For the high ionic strength experiments, leading electrolyte (LE) consisted of 250 mM HCl and 400 mM Tris. For the low ionic strength experiments, the LE was of 10 mM HCl and 20 mM Tris. For both the experiments, terminating electrolyte (TE) was 20 mM HEPES and 40 mM Tris and contained 5 mM of the Analyte MOPS. All chemicals were obtained from Sigma-Aldrich (St. Louis, MO) and diluted from 1 M stock solutions. We also added 1% PVP to both LE and TE to suppress EOF, and added 4 mM $Ba(OH)_2$ (100 mM stock solution) to the TE to precipitate dissolved carbon dioxide [32].

We obtained the fluorescent markers Fluorescein and Oregon Green carboxylic acid (OGCA) from Invitrogen (Carlsbad, CA). We prepared 100 μM concentration stock solution of these fluorescent analytes and diluted their final concentration in the TE. Their respective concentrations were 2 μM and 300 nM for the high ionic strength experiments, and 1 μM and 300 nM for the low ionic strength experiments. We also prepared 1 mM stock solution of the cationic dye rhodamine 6G (R6G, Acros Organics, Geel, Belgium), and used it to visualize the plateau zones of anionic ITP by mixing at a concentration of 100 μM in the LE (see the description of this non-focusing tracer (NFT) in Section 3.3). All solutions were prepared in UltraPure DNase/RNase-free distilled water (GIBCO Invitrogen).

We obtained images using an inverted epifluorescent microscope (IX70, Olympus, Hauppauge, NY) equipped with a mercury lamp, U-MWIBA filter-cube from Olympus (460–490 nm excitation, 515 nm emission and 505 nm cutoff dichroic) and a 10X (NA = 0.4) UPlanApo objective. Images were captured using a 12-bit, 1300 × 1030 pixel array CCD camera (Micromax1300, Princeton Instruments, Trenton NJ). We controlled the camera using Winview32 (Princeton Instruments) and processed the images with MATLAB (R2007b, Mathworks, Natick, MA). We applied constant current (3 and 0.3 μA for the high and low ionic strength cases, respectively) using a high-voltage source-meter (model 2410, Keithley Instruments, Cleveland, OH).

Figure 1 shown in the Supporting Information presents a schematic of the microfluidic chip and ITP injection protocol. We used off-the-shelf microfluidic borosilicate chips (model NS-95) from Caliper Life Sciences (Mountain

View, CA) with channel dimensions 74 μm wide by 12 μm deep. We filled the North, South and West wells (reservoirs) of the chip with LE and applied vacuum to the East well until all channels were filled. We then rinsed the East well several times with distilled water and filled it with the TE, analyte and markers mixture. The electrodes were placed in the East and West wells and constant current was applied. We centered the field of view of the microscope at a fixed distance of 9 mm from the (East) TE well, and set the camera to take images continuously until manually stopped after we observed that an image of the zone was captured.

3 Results and discussions

We integrated the ionic strength model discussed in Sections 1.2 and 1.3 into our existing electrophoresis solver Spresso [7, 31]. The extended Onsager–Fuoss model used in our simulations is the same as that used in Peakmaster [6, 20]. Our presentation here will center on coupling this model to our adaptive-grid electrophoresis solver, and on detailed experimental validations of the related simulations. The ionic strength corrections to mobility and activity coefficients are applied in parallel to the transient simulations of electrokinetic transport equations. As we noted before, many of the physical processes in our code were first represented in Simul [21] (including multispecies electromigration transport of weak electrolytes, a coupling to a mobility and pK_a data base, and ionic strength effects). However, as noted in [21], ionic-strength-dependent calculations are typically computationally intensive, as they are performed for every grid point in the domain, and require an additional set of iterations compared with the zero ionic strength case. This results in significant (and sometimes prohibitive) computational times, limiting the usefulness of uniform-grid solvers (such as Simul) in the design and optimization of electrophoretic separation assays.

The adaptive-grid mechanism in Spresso [7] allows for highly resolved calculations with significantly less grid points (*e.g.* Bercovici *et al.* [7] demonstrated 50-fold decrease in required number of grid points for equivalent resolution at relatively high electric field simulations when compared with a uniform-grid simulation). The number of ionic strength calculations decreases accordingly, resulting in faster solutions. We here also further accelerate the simulations by computing ionic strength effects only when ionic strength at each grid point changes by a particular amount, typically 1%. Together, both features enable efficient computations with ionic strength corrections. This allows for easier comparison of numerical results with experiments, and short turnaround times in the design of electrophoretic assays for researchers and practitioners within the laboratory setting. In this section, we present several examples of the use of the code, and more importantly, provide validation of the code and ionic strength model with experimental results.

The results presented here were obtained using an uncompiled version of the code under Matlab release version R2007b on a 32-bit Windows XP operating system. An AMD Athlon 64 X2 4400+ with 2 GB RAM was used as the computing platform. The chemical properties for all analytes (except fluorescent dyes) were obtained from Hirokawa *et al.* [33]. A list of these chemical properties is built into the graphical user interface of Spresso. For convenience, we provide a Supporting Information table, listing the mobility and relevant pK_a of all the species considered here. With ionic strength corrections, Spresso runs approixmately 100 times faster than Simul. In particular, for the case presented in Fig. 3, for 44 s of simulated time, Simul required 45 000 grid points to provide a non-oscillatory solution which resulted in a computational time of 63 h. For the same case and the same resolution, the combination of an adaptive grid and a moving frame of reference required only 100 grid points in Spresso, leading to a computation time of only 36 min. For the same case, but without ionic strength corrections, Spresso took 16 min of computational time. The source code for Spresso, including linked databases and ionic strength corrections, is provided free of charge at http://www.microfluidics.stanford.edu.

3.1 Effective mobilities

We first benchmarked the calculations for ionic strength corrections for mobility by comparing our model results with Peakmaster [6, 20]. We also validated our model by comparing predicted effective mobilities with experimental results. In the Supporting Information, we present a benchmark of our equilibrium calculations with similar calculations using Peakmaster. Jaros *et al.* [20] compared the results from Peakmaster with experimental values of effective mobilities for several weak acids at different pH, for a small range of ionic strengths between 13 and 20 mM. As ionic strengths of order 100 mM are common in CZE and ITP [26], we here examine electrophoretic mobility of fluorescein for two pH values of 7.15 and 9.35, and ionic strength varying from 30 to 90 mM. The mobility of fluorescein was measured using on-chip capillary electrophoresis. The experimental method and materials are explained in the Supporting Information. Figure 2 shows a comparison between experimental and computed values of effective mobility of fluorescein, as a function of ionic strength. As mentioned in Section 1.2, mobility reduces at higher ionic strengths. The model compares fairly well with experimental values. As expected, at all ionic strengths, the effective mobility at pH 9.35 is higher than that at pH 7.15, as fluorescein is a weak acid ($pK_{a-2} = 6.8$) and thus more strongly disassociated at higher pH.

3.2 Sample preconcentration in peak mode ITP

In ITP, sample ions focus between LE and TE having typically higher and lower effective mobilities, respectively.

''Peak mode'' ITP refers to a focusing mode where the analytes are initially at sufficiently low concentrations (and time of observation sufficiently short) that the analyte does not have enough time to form a plateau zone. In peak mode, analyte ions form a narrow concentrated peak whose width is determined by the diffuse boundaries of neighboring zones (*e.g.* a diffuse boundary between the LE and the TE zones). This type of focusing is common in biological applications such as immunoassays and DNA or RNA separations, where sample concentrations are inherently low [34, 35].

In single-interface injections (*i.e.* a ''semi-infinite sample'' configuration), the sample is mixed in the TE well (reservoir) and continuously overspeeds the TE ions to focus at the TE–LE interface. The TE and sample ions displace the LE ions and, in bulk liquid regions formerly occupied by LE ions, adjust to concentration levels dictated by the LE [19]. The sample concentration, $C_{S,te}$, in the new ''regulated'' TE zone can be calculated from flux balance at the interface of TE well and regulated TE zone. $C_{S,te}$ is related to the initial sample concentration $C_{S,te\,well}$ as [19]

$$C_{S,te} = \frac{\mu_{S,te\,well}}{\mu_{S,te}} \frac{\mu_{T,te}}{\mu_{L,le}} \frac{\sigma_{le}}{\sigma_{te\,well}} C_{S,te\,well} \tag{11}$$

where $\mu_{S,te\,well}$ and $\mu_{S,te}$ are the effective mobilities of the sample ions in the TE well and the regulated TE zone, and $\mu_{T,te}$ and $\mu_{L,le}$ are the effective mobilities of the TE ions in the regulated TE zone and LE ions in LE zone. σ_{le} and $\sigma_{te\,well}$ represent the conductivities of the LE zone and the TE well.

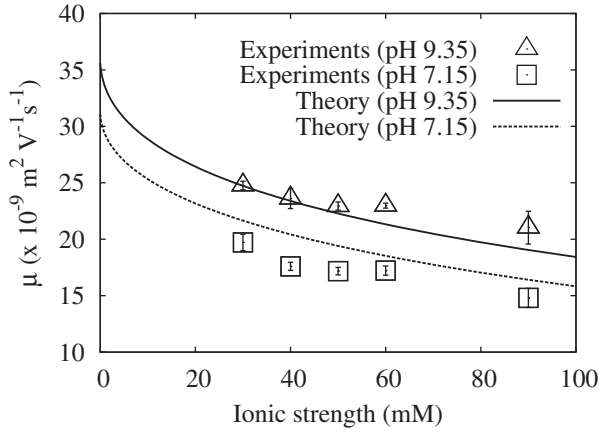

Figure 2. Effect of ionic strength on ionic mobility of Fluorescein at two pH values. Data show the experimentally measured ionic mobility of fluorescein. Squares and triangles correspond to measurements obtained at pH 7.15 and 9.35, respectively. Measurements were made by CZE, using glycine-sodium hydroxide buffer at pH 9.35 and HEPES-sodium hydroxide buffer for pH 7.15. Plotted uncertainty bars correspond to 95% confidence in mean values, calculated using Student's *t*-test distribution. The trends provided by numerical calculations (lines) agree fairly well with other experimental observations (see the Supporting Information). Calculations were obtained using $\mu^0_{-1} = -19 \times 10^{-9}\,m^2/V/s$, $pK_{a-1} = 4.4$ and $\mu^0_{-2} = -36 \times 10^{-9}\,m^2/V/s$, $pK_{a-1} = 6.8$.

The amount of sample accumulated in peak mode, N_s, depends primarily on the ratio of the effective mobility of the analyte in the TE zone to that of the TE anion in the TE zone, the initial sample concentration, and the time elapsed between injection and detection. The rate of accumulation with respect to the distance traveled by the interface (neglecting EOF) is given by [19].

$$\frac{dN_s}{dx} = \frac{dN_s}{dt}\frac{1}{dx/dt} = \frac{dN_s}{dt}\frac{1}{V_{ITP}} = \left(\frac{\mu_{S,te}}{\mu_{T,te}} - 1\right) C_{S,te} \tag{12}$$

where $V_{ITP} = \mu_{L,le} j/\sigma_{le}$ is the speed of ITP front. $\mu_{L,le}$ and σ_{le} are the effective mobility of LE ions and conductivity of LE zone, respectively. At low ionic strengths, sample concentration in the TE zone increases proportionally with LE concentration (conductivity) as *per* Eq. (11). As a result, from Eq. (12), focusing rate of sample increases with increase in LE concentration. However, Eqs. (2) and (3) show that a divalent ion experiences greater reduction in mobility than a univalent ion as ionic strength is increased. For univalent TE ions and divalent sample ions, the ratio $\mu_{S,te}/\mu_{T,te}$ in (12) therefore decreases with increasing ionic strength (Eq. 3). Thus, the focusing rate of a divalent sample initially increases with increasing ionic strength in the low ionic strength regime (as *per* the $C_{S,te}$ factor in Eq. 12) but then decreases at higher ionic strengths as $\mu_{S,te}/\mu_{T,te}$ decreases. The net result is that for a divalent sample ion, the focusing rate increases with LE conductivity at low ionic strengths but then saturates and decreases with further increase of ionic strength.

Khurana and Santiago [19] experimentally observed reduction in focusing rate for divalent Alexa–Fluor 488 (AF) ions in peak mode ITP. Their experimental data values are shown as circles in Fig. 3. We here compare the predictions of sample accumulation in peak mode ITP obtained from time-dependent numerical simulations in Spresso with the experimental observations of Khurana and Santiago [19]. Figure 3a shows numerical predictions of accumulated moles of AF as a function of LE concentration for calculations performed with (solid line) and without (dashed line) ionic strength correction. As Khurana and Santiago [19] pointed out, the sample concentration in the adjusted TE zone increases with increased LE concentration in accordance with Eq. (11). However, at sufficiently high ionic strength, the mobility of the divalent sample (AF) decreases more strongly than that of the univalent TE (3-phenylpropionic acid). This results in decreased accumulation of AF at higher ionic strengths, such that the accumulated moles reach maximum (at $\sigma_{le} = 2$ S/m) and decrease for higher LE conductivities.

In the inset of Fig. 3, we plot the same AF accumulated amount data as the main plot but here as a function of LE concentration to further highlight the effect of neglecting ionic strength corrections in ITP simulations. The predictions obtained by considering ionic strength effects (solid curve) agree well with experimental observations (circles). However, the simulations that neglect ionic strength corrections (dotted curve in both inset and main plot) are

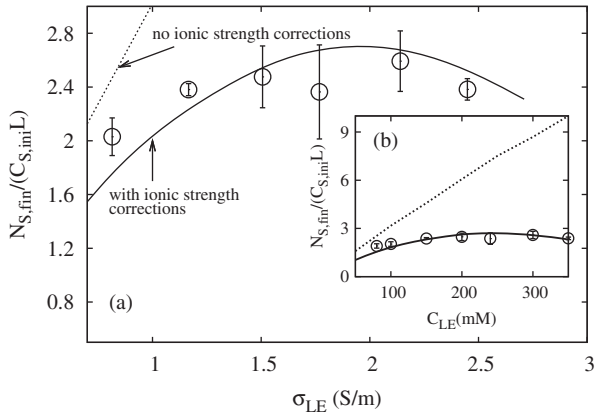

Figure 3. Influence of ionic strength dependence on a divalent analyte focusing in peak mode ITP (with univalent TE). (a) Experimental validation of the ionic strength dependence model showing the moles of accumulated sample at an LE-TE interface *versus* the conductivity of the LE. Circles show experimental data [19], while the solid line shows numerical which take into account the effect of ionic strength. The dotted line shows predicted sample accumulation when ionic strength effects are neglected. Inset (b) shows a comparison with the same data but now *versus* LE concentration. This highlights the discrepancy in simulated sample accumulation predicted with (solid line) and without (dotted line) ionic strength correction. The analyte is 10 nM AF initially mixed with the TE. LE is histidine-HCl (500 mM stock solution, pH = 4.3) and TE is 3-phenylpropionic acid (50 mM stock solution titarted with NaOH to pH = 4.9). All of the computational results shown use identical conditions.

clearly inaccurate above about 50 mM LE concentrations. These predictions do not take into account the reduced mobility of AF relative to TE ions at sufficiently high ionic strength and grossly overpredict the trend with increasing LE concentration.

We note that the strong effect of ionic strength shown in Fig. 3 is not expected for univalent sample ions with univalent TE co-ion. Our simulations show that, for a hypothetical univalent ion with a limiting mobility equal to that of AF, the accumulated moles in peak mode ITP follow the dotted curve in Fig. 3b, irrespective of whether ionic strength effects are taken into account. This is because the effect of decreased mobility of univalent sample at high ionic strength is offset by the decrease in the mobility of univalent TE ions.

3.3 Simulation of mobility markers in ITP in regimes where ionic strength is important

Khurana and Santiago [36] proposed a technique for indirect detection of unlabeled non-fluorescent analytes using fluorescent markers in ITP. A set of fluorescent markers are initially mixed with the sample analytes. The markers are chosen to have specific mobilities so that they focus (typically in peak mode) at the interfaces between analyte zones. The unlabeled analytes are then detected as gaps in the fluorescence signal. The technique is effective, provided the effective mobilities of the fluorescent markers bracket those of analytes of interest. The technique eliminates the need for labeling (and directly detecting) analyte ions. The choice of correct chemistry and fluorescent markers for a given analyte is crucial.

We here demonstrate the effect of ionic strength on the indirect detection of an analyte using the mobility markers technique. We examine the case of the detection of a single analyte, MOPS, using the fluorescent markers OGCA and Fluorescein. The LE and TE used in this example are Tris-HCl and Tris-HEPES, respectively. The compositions of LE and TE for each case are given in Section 2. Each of the four plots in Fig. 4 shows both simulation (foreground curves) and experimental results (background). Figures 4A and B show results for a high ionic strength (250 mM), while Figs. 4C and D show results for low ionic strength (10 mM). The experimental data in the two plots of the left column (Figs. 4A and C) show results using the NFT technique [37]. The NFT used was 100 μM R6G, which was mixed with LE. R6G is a cation and does not focus. Instead its concentration (which is negligible and does not appreciably contribute to local conductivity) adapts according to local electric field in the various ITP zones. Figures 4A and C also show simulations results which can be compared qualitatively with the NFT measurements. The experimental data in Figs. 4B and D (right column) are direct measurements of the fluorescence of analytes in peak mode. Shown with the latter are simulations of the concentration of these analytes.

The experimental data of Figs. 4A and C confirm the existence of an MOPS zone. At both ionic strengths, the MOPS zone has significant width and is clearly made visible by the NFT as it migrates from LE to TE. The MOPS zone forms a ''spacer'' ion between the LE and the TE, and the Fluorescein mobility marker focuses either in front of or behind the MOPS, as dictated by the ionic strength of the LE.

Figure 4B shows the experimental and simulation data indicative of the concentration of the two mobility markers for the 250 mM ionic strength, Fluorescein and OGCA here focus, respectively, behind and in front of the MOPS zone. The two mobility marker peaks thus indicate the presence of an analyte (MOPS) between them. Simulated signal peaks for both OGCA and Fluorescein agree well with the experimental fluorescence signal; Fig. 4D shows experimental and simulation results for the 10 mM case. In both the cases, OGCA and Fluorescein focus ahead of the MOPS zone (and behind the LE) and are so detected as a single peak in the experiment. Fluorescein is a divalent ion and so its mobility has a stronger dependence on ionic strength than the monovalent MOPS zone. Here, therefore, the mobility markers OGCA and Fluorescein focus in the same region and fail to detect the presence (*via* a gap) and concentration (*via* the zone width) of the MOPS ion. The simulations do well in predicting this effect and aid a user to design a successful mobility marker experiment.

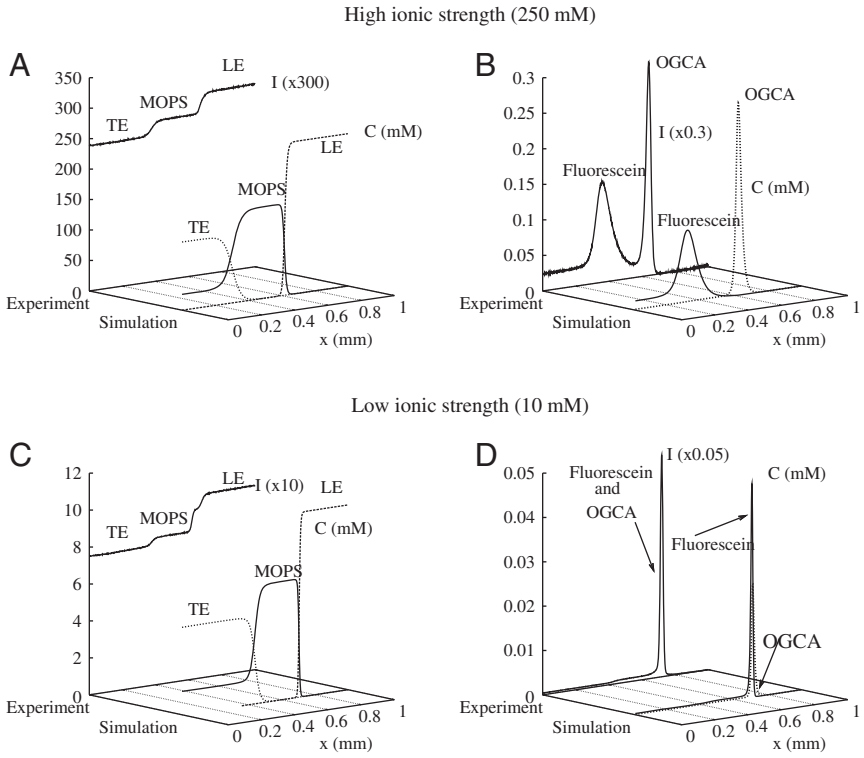

Figure 4. Comparison of numerical and experimental results of separation and detection of sample analytes, using NFT and fluorescent mobility markers at high (A, B) and low ionic strength (C, D). In (A), the analyte MOPS forms a plateau zone between LE and TE. Simulated zones compare well with experimental NFT data. (B) The calculated concentration and measured intensity of the fluorescent markers Fluorescein and OGCA at the two interfaces of the MOPS zone. The two distinct peaks show that Fluorescein focuses behind MOPS, as predicted by numerical simulations. In (C), low ionic strength experiments and simulations show that the analyte MOPS also form a plateau zone between LE and TE. (D) The measured fluorescence intensity yielding a single peak, in agreement with the simulation. At 10 mM ionic strength the mobility of the divalent Fluorescein is substantially higher and hence both Fluorescein and OGCA markers focus ahead of MOPS. These markers are thus unable to detect the MOPS plateau. For simulations, chemical properties of OGCA were taken to be $\mu^0_{-1} = -43 \times 10^{-9}$ m^2/V/s and $pK_{a-1} = 4.7$. Properties of Fluorescein were the same as those used in Section 3.1.

We note that all of the experiments of Fig. 4 were performed at a pH of about 8, at which all species are (to good approximation) fully ionized. Thus, these results are indeed primarily indicative of mobility reduction due to ionic strength (*e.g.* Eq. 3). In addition, we note that we suspect the small zone between MOPS and LE in Fig. 4C was carbonic acid, known to be present at substantial concentrations at the pH of the experiment [28] (despite our use of $Ba(OH)_2$ in the TE). This hypothesis was supported by experiments where we varied the amount of $Ba(OH)_2$ (increasing $Ba(OH)_2$ showed reductions in the zone width of this zone between MOPS and LE).

3.4 Selectivity changes in CZE at varying ionic strength

Ionic strength effects can also lead to fundamental changes in CZE electropherogram signals. Changes in peak shape and selectivity resulting from changes in ionic strength in CZE have been observed experimentally by [38]. Electrophoretic separations at varying ionic strength can also exhibit changes of peak order [39]. Harrold *et al.* [16] showed experimentally the effect ionic strength on selectivity of inorganic anions in capillary electrophoresis. We here present simulations based on experimental conditions of Harrold *et al.* [16]. To this end, we present two simulations of the electrophoretic separation of chloride, fluoride, sulfate and phosphate ions using sodium tetraborate buffer at pH 9.2, at 1 and 5 mM ionic strengths. The separations leveraged EOF with a mobility greater than and in direction opposite to the electrophoretic mobility of anions to achieve net migration toward the cathode. We incorporated into our simulations the EOF associated with these experiments (we determined the EOF mobility from a noticeable system peak in their measurements).

Figure 5 shows a plot of the experiments of Harrold *et al.* [16] along with our associated simulations. For this anionic CZE with dominant EOF, ions with highest electrophoretic mobility reach the detector last. At low ionic strength (1 mM), the experiments show phosphate (HPO_4^{2-}) is barely resolved relative to fluoride (F^-). In addition, sulfate (SO_4^{2-}) is not resolved relative to the chloride (Cl^-) ion. F^-, HPO_4^{2-}, Cl^- and SO_4^{2-} reach the detector, respectively with ascending order of migration times. The simulations capture well the shape of electropherogram including the poor resolution between the two ion pairs and the reported order of elution.

Figure 5 (right side) also shows the experiment *versus* simulation comparisons for (the higher) ionic strength of 5 mM (again at pH = 9.2). At these conditions HPO_4^{2-} reaches the detector followed successively by F^-, SO_4^{2-} and Cl^- ions. Thus the order of F^- and HPO_4^{2-} is reversed, as is the order of the Cl^- and SO_4^{2-} peaks. Further, the experiment shows that the Cl^- and SO_4^{2-} peaks changed order and are now well resolved. Again, the simulation well captures the electropherogram shape including the peak order reversal and improved resolution.

The electropherogram shape is determined by the relative mobility of these anions. At low ionic strength, the small electrophoretic mobility difference between Cl^- and SO_4^{2-} makes them difficult to resolve. However, the divalent SO_4^{2-} ion has a more strongly shielding ionic atmosphere than the univalent Cl^- ion, hence SO_4^{2-} experiences greater decrease in mobility with increasing ionic strength. This yields good resolution of these ions at the higher ionic strength. This increased sensitivity of the divalent ion mobility (relative to monovalent) to ionic strength also explains the order reversal in each of the two ion pairs. Overall, our simulations well capture these effects and show very good qualitative agreement with the experimental observations of Harrold *et al.* [16]. We attribute small discrepancies between the data and the simulations to the effects of EOF (which affects both placement and relative width of peaks).

4 Concluding remarks

We have developed and experimentally validated electrophoresis (open source) solver that includes the effects of ionic strength on both fully ionized mobility of and activity coefficients for weak electrolytes. The solver provides fast, accurate solutions for separation and focusing assays including CZE and ITP. The simulations use Onsager–-Fuoss correction [9] for fully ionized electrophoretic mobility and extended Debye–Huckle theory [22] for correction of ionic activity. We use these models to understand and interpret experimental observations at low and high ionic strengths. Simulations show and experiments confirm reduced sample preconcentration for multivalent ions, in peak mode ITP, at high ionic strengths. This occurs because multivalent ions attract a stronger counter-ion atmosphere, which leads to greater shielding of applied electric field and ion-drag-induced reductions in electrophoretic mobility. Mobility of highly charged ions reduces faster compared with univalent ions, as ionic strength is increased. This can lead to fundamental changes in CZE and ITP peak/zone shape and order. We compared our simulations to experimental measurements to show that they can predict qualitative changes such as zone order in ITP and CZE experiments.

Our solver uses faster numerical schemes and all cases were simulated with the same conditions as experiments. Such simulations can be employed for practical use in minimizing experimental trials and for determining the optimal choice of assay conditions including ionic strength, pH and buffer types. Here, we demonstrated the use of simulations for designing a successful a mobility marker assay [36] and in demonstrating a reversal in the order of sample peaks in CZE. Simulations which appropriately account for the effects of ionic strength can be important also in designing (*e.g.* CZE or ITP) experiments using

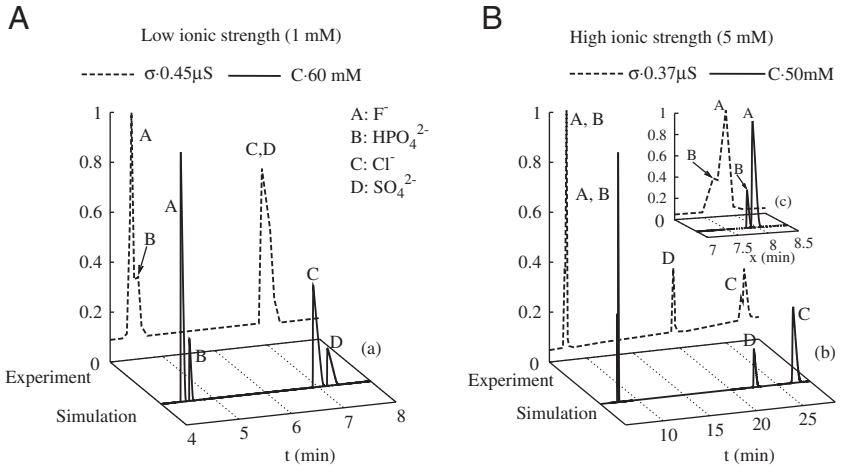

Figure 5. Experiments from Harrold *et al.* [16] and our respective simulations showing the effect of ionic strength dependence on electropherograms (from CZE) of four ions. (a) At 1 mM ionic strength, both experiments and simulations show Cl^- is not well resolved from SO_4^{2-}, and HPO_4^{2-} is not well resolved from F^-. (b) At 5 mM ionic strength, the simulations capture the strong documented effect of ionic strength. Here, we see the order of the Cl^- *versus* SO_4^{2-} and HPO_4^{2-} *versus* F^- are reversed. Further, the experiments and simulations show that the Cl^- is now very well resolved from SO_4^{2-}. Inset (c) shows magnified view of the F^-/HPO_4^{2-} peak pair. The 1 and 5 mM cases were each sodium tetraborate at pH 9.2. For all simulations, concentrations of anions were: 27 μM Cl^-, 10 μM SO_4^{2-}, 50 μM F^- and 10 μM HPO_4^{2-}. In both the cases, a 60 cm long capillary with 75 μm inner diameter was used. Simulations and experiments used constant voltage of 24 kV. For the sake of comparison, the values of σ and C are scaled by factors shown in plot to fit the same axes.

conductivity detection, where signal strength and shape itself is a strong function of ionic strength.

S. S. B. is supported by Stanford School of Engineering Fellowship and Mayfield Stanford Graduate Fellowship. M. B. is supported by an Office of Technology Licensing Stanford Graduate Fellowship and a Fulbright Fellowship. The authors thank Tarun Khurana and Denitsa Milanova for sharing their experimental data. They gratefully acknowledge support from the Micro/Nano Fluidics Fundamentals Focus (MF3) Center funded by Defense Advanced Research Projects Agency (DARPA) MTO Grant No. HR0011-06-1-0050 and contributions from MF3 corporate members.

The authors have declared no conflict of interest.

5 References

[1] Simpson, S. L., Jr., Quirino, J. P., Terabe, S., *J. Chromatogr. A* 2008, *1184*, 504–541.

[2] Chen, L., Prest, J. E., Fielden, P. R., Goddard, N. J., Manz, A., Day, P. J. R., *Lab Chip* 2006, *6*, 474–487.

[3] Beckers, J. L., Everaerts, F. M., Ackermans, M. T., *J. Chromatogr. A* 1991, *537*, 407–428.

[4] Friedl, W., Kenndler, E., *Anal. Chem.* 1993, *65*, 2003–2009.

[5] Gluck, S. J., Cleveland, J. A., Jr., *J. Chromatogr. A* 1994, *680*, 49–56.

[6] Gas, B., Coufal, P., Jaros, M., Muzikar, J., Jelinek, I., *J. Chromatogr. A* 2001, *905*, 269–279.

[7] Bercovici, M., Lele, S. K., Santiago, J. G., *J. Chromatogr. A* 2009, *1216*, 1008–1018.

[8] Persat, A., Suss, M. E., Santiago, J. G., *Lab Chip* 2009, *9*, 2454–2469.

[9] Onsager, L., Fuoss, R. M., *J. Phys. Chem.* 1932, *36*, 2689–2778.

[10] Pitts, E., *Proc. R. Soc. Lond. A* 1953, *217*, 43–70.

[11] Bockris, J. O'M., Reddy, A. K. N., *Modern Electrochemistry 1: Ionics*, 2nd Edn, Plenum Press, New York 1998.

[12] Robinson, R. A., Stokes, R. H., *Electrolyte Solutions*, 2nd Revised Edn, Dover Publications, New York 2002.

[13] Porras, S. P., Riekkola, M., Kenndler, E., *Electrophoresis* 2003, *24*, 1485–1498.

[14] Sustacek, V., Foret, F., Bocek, P., *J. Chromatogr.* 1991, *545*, 239–248.

[15] Bushey, M. M., Jorgenson, J. W., *J. Chromatogr.* 1989, *480*, 301–310.

[16] Harrold, M., Stillian, J., Bao, L., Rocklin, R., Avdalovic, N., *J. Chromatogr. A* 1995, *717*, 371–383.

[17] Everaerts, F. M., Beckers, J. L., Verheggen, Th. P. E. M., *Isotachophoresis – Theory, Instrumentation and Applications*, Elsevier, Amsterdam 1976.

[18] Friedl, W., Reijenga, J. C., Kenndler, E., *J. Chromatogr.* 1995, *709*, 163–170.

[19] Khurana, T. K., Santiago, J. G., *Anal. Chem.* 2008, *80*, 6300–6307.

[20] Jaros, M., Vcelakova, K., Zuskova, I., Gas, B., *Electrophoresis* 2002, *23*, 2667–2677.

[21] Hruska, V., Jaros, M., Gas, B., *Electrophoresis* 2006, *27*, 984–991.

[22] Debye, P., Huckel, E., *Physik. Z.* 1923, *24*, 305–325.

[23] Onsager, L., *Phys. Z.* 1926, *27*, 388–392.

[24] Onsager, L., *Phys. Z.* 1927, *28*, 277–298.

[25] Debye, P., Huckel, E., *Physik. Z.* 1923, *24*, 185–206.

[26] Li, D., Fu, S., Lucy, C. A., *Anal. Chem.* 1999, *71*, 687–699.

[27] Gebauer, P., Bocek, P., *J. Chromatogr.* 1984, *299*, 321–330.

[28] Khurana, T. K., Santiago, J. G., *Lab Chip* 2009, *9*, 1377–1384.

[29] Saville, D. A., Palusinski, O. A., *AIChE J.* 1986, *32*, 207–214.

[30] Stědrý, M., Jaros, M., Hruska, V., Gas, B., *Electrophoresis* 2004, *25*, 3071–3079.

[31] Bercovici, M., Lele, S. K., Santiago, J. G., *J. Chromatogr. A* 2010, *1217*, 588–599.

[32] Persat, A., Chambers, R. D., Santiago, J. G., *Lab Chip* 2009, *9*, 2437–2453.

[33] Hirokawa, T., Nishino, M., Kiso, Y., *J. Chromatogr.* 1982, *252*, 49–65.

[34] Schoch, R. B., Ronaghi, M., Santiago, J. G., *Lab chip* 2009, *9*, 2145–2152.

[35] Lin, C. C., Hsu, B. K., Chen, S. H., *Electrophoresis* 2008, *29*, 1228–1236.

[36] Khurana, T. K., Santiago, J. G., *Anal. Chem.* 2008, *80*, 279–286.

[37] Chambers, R. D., Santiago, J. G., *Anal. Chem.* 2009, *81*, 3022–3028.

[38] Mechref, Y., Ostrander, G. K., El Rassi, Z., *J. Chromatogr. A* 1997, *792*, 75–82.

[39] Reijenga, J. C., Verheggen, T. P. E. M., Martens, J. H. P. A., Everaerts, F. M., *J. Chromatogr. A* 1996, *744*, 147–153.

